US Army Corps of Engineers®

U.S. ARMY

ERDC

Cold Regions Research and Engineering Laboratory

Experimental and Numerical Analyses of Soil Electrical Resistivity under Subfreezing Conditions

Rui Liu, Cheng Zhu, John Schmalzel, Daniel Offenbacker, Yusuf Mehta, Benjamin Barrowes, Danney Glaser, and Wade Lein

April 2024

Experimental and Numerical Analyses of Soil Electrical Resistivity under Subfreezing Conditions

Benjamin Barrowes, Danney Glaser, and Wade Lein

US Army Engineer Research and Development Center (ERDC)
Cold Regions Research and Engineering Laboratory (CRREL)
72 Lyme Road
Hanover, NH 03755-1290

Rui Liu, Cheng Zhu, Daniel Offenbacker, and Yusuf Mehta

Rowan University
Center for Research and Education in Advanced Transportation Engineering Systems (CREATEs)
Department of Civil and Environmental Engineering
201 Mullica Hill Road
Glassboro, New Jersey 08028

John Schmalzel

Rowan University
Department of Electrical and Computer Engineering
201 Mullica Hill Road
Glassboro, New Jersey 08028

Final Report

Abstract

The engineering behavior of frozen soils is critical to the serviceability of civil infrastructure in cold regions. Among various geophysical techniques, electrical resistivity imaging is a promising technique that is cost effective and provides spatially continuous subsurface information. In this study, under freeze–thaw conditions, we carry out lab–scale 1D electrical resistivity measurements on frost–susceptible soils with varying water content and bulk density properties. We use a portable electrical resistivity meter for temporal electrical resistivity measurements and thermocouples for temperature monitoring. Dynamic temperature-dependent soil properties, most notably unfrozen water content, exert significant influences on the observed electrical resistivity. Below 0 °C, soil resistivity increases with the decreasing temperature. We also observe a hysteresis effect on the evolution of electrical resistivity during the freeze–thaw cycle, which effect we characterize with a sigmoidal model. At the same temperature, electrical resistivity during freezing is consistently lower than that during thawing. We have implemented this sigmoidal model into a COMSOL finite element model at both laboratory and field scales which enables the simulation of soil electrical resistivity response under both short–term and long–term sub–freezing conditions. Atmospheric temperature variations induce soil temperature change, and thereby phase transition and electrical resistivity change, with the rate of change being a function of the depth of investigation and soil properties include initial water content and initial temperature. This study advances the fundamental understanding of the electrical behaviors of frozen soils and enhance the application of electrical geophysical investigations in cold regions.

Preface

This page intentionally left blank.

Experimental and numerical analyses of soil electrical resistivity under subfreezing conditions

1. Introduction

Frozen soils are widely distributed across the globe. More than 50% of the uppermost soils in the Norther Hemisphere are seasonally frozen (Zhang et al., 2002). Permafrost soils, referring to soils that remain frozen for more than two consecutive years, are predominantly found in the Arctic and sub–Arctic regions such as Greenland, Northern Canada, and Alaska (Harris, 2018). Moreover, frozen soils also commonly exist in plateau areas, such as Qinghai–Xizang (Tibetan) Plateau, China (Zhao et al., 2004). Engineering hazards associated with frozen soils have garnered increasing attention in recent decades, as the aging infrastructure in the United States becomes more vulnerable and rising temperatures in the Northern Hemisphere make frozen ground more unstable.

Under seasonal weather change and global warming effect, this wide presence of frozen soils has imposed numerous and pressing challenges to the design, construction, and maintenance of various types of infrastructure. When temperature decreases, the freezing and subsequent phase change of pore water into ice causes surface heave, which may significantly damage the overlying infrastructure (Kouretzis et al., 2015; Merifield et al., 2009). On the other hand, when temperature increases, the thaw weakening of subsurface soils may induce excessive settlement

Table 1
Summary of electrical resistivity models developed for frozen soil.

Model	Symbol	Unit	Explanation	Reference
$\rho^{-1} = \frac{n}{\tau^2\rho_w}\frac{\left(\int_{Dmin}^{Dmax}\frac{f(D)dD}{D^2}\right)^2}{\int_{Dmin}^{Dmax}\frac{f(D)dD}{D^4}} + \frac{4n}{\tau^2\rho_s}\frac{\left(\int_{Dmin}^{Dmax}\frac{f(D)dD}{D^2}\right)^2}{\int_{Dmin}^{Dmax}\frac{f(D)dD}{D^3}}$	ρ	$\Omega\cdot m$	Electrical resistivity of the soil matrix	(Ming et al., 2020)
	n	/	Porosity	
	τ	/	Pore tortuosity, can be estimated as $\tau = 1 + 0.41ln\left(\frac{1}{n}\right)$	
	ρ_w	$\Omega\cdot m$	Electrical resistivity of pore water	
	ρ_s	$\Omega\cdot m$	Electrical resistivity of solid	
	$Dmax$	m	Maximum pore diameter	
	$Dmin$	m	Minimum pore diameter	
	D	m	Pore diameter in probabilistic distribution	
$\rho = \left[A \times \frac{a\theta^{-b}}{w} + \rho_d\left(B \times \frac{a\theta^{-b}}{w} + C\right) + D\right]^{-1}$	ρ	$\Omega\cdot m$	Electrical resistivity of soil matrix	(Shan et al., 2017)
	A, B, C, D, a, b	/	Coefficients from experiments	
	$a\theta^{-b}$	/	Unfrozen water content	
	θ	$°C$	Absolute value of soil temperature	
	w	/	Total water content	
	ρ_d	$g\cdot cm^{-3}$	Dry density	
$\rho = m\theta_u^n$	ρ	$\Omega\cdot m$	Electrical resistivity of soil matrix	(Tang et al., 2018)
	m	/	Coefficient from experiments	
	θ_u	/	Unfrozen water content	
	n	/	Coefficient from experiments	
$\rho_{bulk}^T = \frac{\phi^{1-m}}{\sigma_w^{T_0}\phi^{T_0}(1-\alpha(T_0-T))}$	ρ_{bulk}^T	$\Omega\cdot m$	Electrical resistivity of soil matrix at temperature T	(Wu et al., 2017)
	ϕ	/	Porosity	
	m	/	Coefficient from experiments	
	$\sigma_w^{T_0}$	S/m	Electrical conductivity of pore water at temperature T_0	
	ϕ^{T_0}	/	Porosity at temperature T_0	
	α	$°C^{-1}$	Water conductivity temperature coefficient	
	T_0	$°C$	Reference temperature	
	T	$°C$	Temperature under frozen state	
$\rho_{bulk,T<0} = \frac{S_r^{1-n}}{[0.159C_0[d(0-25)+1]]a^{-1}\phi^m S_{w0}^n}$	$\rho_{bulk,\ T<0}$	$\Omega\cdot m$	Electrical resistivity of soil matrix at temperature T	(Herring et al., 2019)
	S_r	/	Water saturation	
	m	/	Coefficient from experiments	
	n	/	Coefficient from experiments	
	C_0	$g\cdot L^{-1}$	Concentration of pore fluid	
	d	$°C^{-1}$	$d = 0.02\ °C^{-1}$	
	a	/	Coefficient from experiments	
	ϕ	/	Porosity	
	S_{w0}	/	Initial water saturation	
$\rho = \frac{\alpha\rho_w\theta^{-m}S_w^{-n}}{1+\alpha_t(T-T_0)}$	ρ	$\Omega\cdot m$	Electrical resistivity of soil matrix	(Briggs et al., 2017)
	α, m, n	/	Coefficients from experiments	
	ρ_w	$\Omega\cdot m$	Electrical resistivity of pore water	
	θ	/	Porosity	
	S_w	/	Water saturation at temperature T_0	
	α_t	K^{-1}	Temperature coefficient 0.025 K^{-1}	
	T	K	Temperature under frozen state	
	T_0	K	Reference temperature	
$\rho^{-1} = \frac{S_l n\sigma_l}{\alpha_l + c_l S_l n\sigma_l} + \frac{S_i n\sigma_i}{\alpha_i + c_i S_i n\sigma_i}$	ρ	$\Omega\cdot m$	Electrical resistivity of soil matrix	(Mao et al., 2016)
	S_l, S_i	/	Water saturation in water and ice phase	
	n	/	Porosity	
	σ_l, σ_i	S/m	Electrical conductivity of water and ice phase	
	α_l, α_i	/	Structure factor of water and ice phase	
	c_l, c_i	/	Coefficients from experiments	
$\rho = \frac{a_1}{1+e^{-b_1(T-c_1)}}$	ρ	$\Omega\cdot m$	Electrical resistivity	(Lyu et al., 2019)
	a_1, b_1, c_1	/, /, $°C$	Fitting parameters	
	T	$°C$	Temperature	

(Hong et al., 2014; Ma et al., 2012; Sun et al., 2018). Moreover, global warming has further accelerated these physical changes in soil, especially in the cold regions (Chapman and Walsh, 2007), imposing additional threats to local infrastructure, such as pavements and roadways (AzariJafari et al., 2018). This highlights the importance of the characterization of frozen soils subjected to freeze-thaw thermal paths.

To investigate the physical properties of frozen soils in the field, various techniques have been developed. Traditional ground survey techniques such as drilling and standard penetration test are destructive and provide discrete information of soil at selected sites only. Moreover, higher operational costs are usually needed for boring in frozen grounds (Kneisel et al., 2008). Non–destructive geophysical investigations are relatively cost–effective and provide spatially continuous subsurface information. Among them, electrical resistivity imaging (ERI) has shown promising applications in agriculture (Samouëlian et al., 2003), geology (Briggs et al., 2017), geophysics (Gance et al., 2016; Hauck, 2002), and civil engineering (Rucker et al., 2009). Due to its ability to monitor soil water content (Zhou et al., 2001), characterize soil property (e.g., strength) (Hauck, 2002; Sudha et al., 2009), and detect soil crack detection (Samouëlian et al., 2003), ERI has been applied for assessing landslide zones, mapping Karst caves, and monitoring subsurface moisture flow (Ahmed et al., 2017; Gan et al., 2020; Glaser et al., 2005).

Theoretical calculation of soil electrical resistivity is normally given by Archie's law (Archie, 1942), where the degree of saturation, pore fluid concentration, and porosity are considered as influencing factors (Glover, 2010; Glover, 2017; Han et al., 2021). Other laboratory studies confirm relationships between the electrical resistivity of a soil and its physical properties. For example, Komine (1997) found that sands with larger pores sizes had larger electrical resistivity values compared to those with smaller pore sizes. Sreedeep et al. (2005) observed exponential relationships between soil electrical resistivity and the degree of saturation. Liu et al. (2008) reported a monotonic relationship between electrical resistivity and unconfined compressive strength in soil–cement mixtures. Zhang et al. (2014) showed a decrease to one fourth of
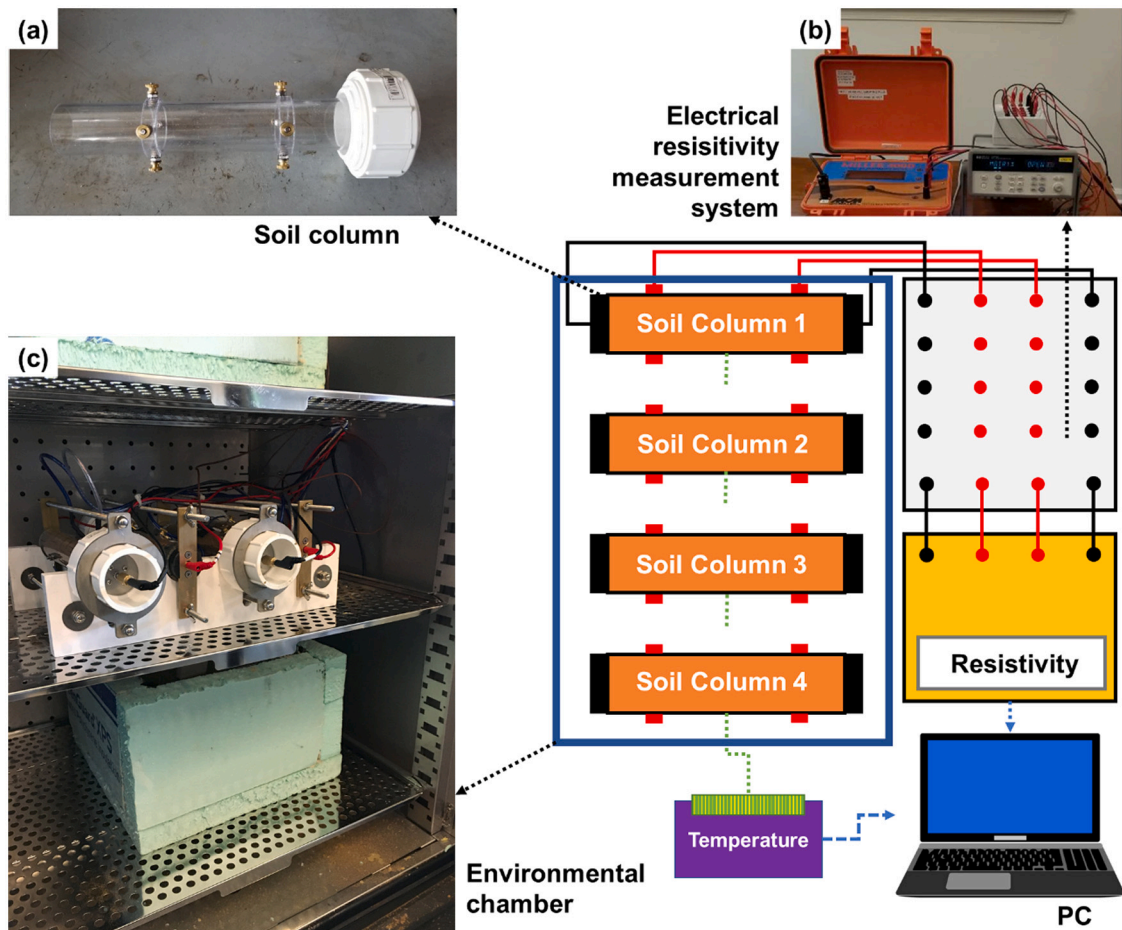
Fig. 1. Schematic view of the experimental setup: (a) soil column with arcrylic container and metal electrodes on both ends and side wall; (b) electrical resistivity measurement system integrated with multi-switch to enable simultaneous measurement of multiple soil columns; and (c) environmental chamber used to provide low temperature conditions for soil columns.

the original resistivity value when salt concentration increased from 2.5% to 10.0% by weight in clays. For frozen soils, electrical resistivity is heavily dependent the unfrozen water content (Oldenborger and LeBlanc, 2018), which represents the actual portion of liquid phase in the soil. To estimate unfrozen water content in the soil, soil freezing characteristic curve is introduced to illustrate the relationship between unfrozen water content and temperature (Bai et al., 2018), so measurement on soil temperature can show some indicators of changes in unfrozen water content.

Despite extensive laboratorial measurements of soil electrical resistivity conducted at room temperature, the investigation of soils under subzero temperature remains limited. To fill this research gap, recent years have witnessed more studies on the geoelectrical properties of frozen soils and showed their strong dependence on soil properties. Wu et al. (2013, 2017) have investigated freeze–thaw transitions (−20 °C ∼ 4 °C) in arctic soils, where single frequency induced polarization responses were found to be exclusively related to the unfrozen water content. Lyu et al. (2019) established a power function relationship between the salinity of pore fluid and electrical resistivity in frozen soils. Ming et al. (2020) investigated the electrical resistivity of frozen clay and its dependence on soil pore structure. Sun et al. (2020) discovered changing correlations between the electrical resistivity and thermal conductivity of soil at different temperatures (−20 °C ∼ 10 °C). These studies discussed the dependence of soil electrical resistivity on its various physical properties under monotonically changing temperature. However, the geoelectrical behavior of frozen soils under the freeze/ thaw cycles remains unclear. Moreover, in most previous works,

although the experimental data representing the evolution of soil electrical resistivity could be fitted, those fitting models do not fully consider hysteresis under freeze-thaw cycles. More importantly, hysteresis in electrical resistivity has been observed when comparing the freezing and thawing paths.

In this work, we studied the effects of sub–freezing temperature regime on the electrical resistivity of frost–susceptible soils. We prepared soil column samples with different densities and initial water contents, and monitored their electrical resistivity evolution during one freeze-thaw cycle (between −15 and 15 °C) using the Wenner four––electrode method. A finite element model was developed to investigate the influence of environmental temperature on the electrical responses of soils under freeze–thaw conditions. Short-term and long-term simulation results from the model reveal the spatiotemporal evolution of the soil temperature field and the dynamic soil electrical resistivity responses.

2. Electrical resistivity models for frozen soils: State of the art

This section provides a review of existing theoretical electrical resistivity models developed for frozen soils. These models show the dependence of the electrical resistivity of frozen soils on various influencing factors (Table 1), such as environmental conditions (e.g., temperature) and soil properties (e.g., water content, porosity, density). Some of these models were formulated based on the intrinsic relationship between electrical properties and soil structure, such as those developed by Tang et al. (2018) and Mao et al. (2016). Certain model
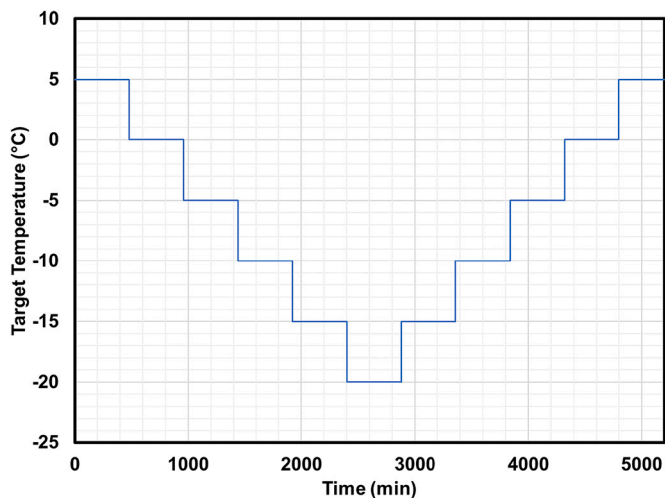
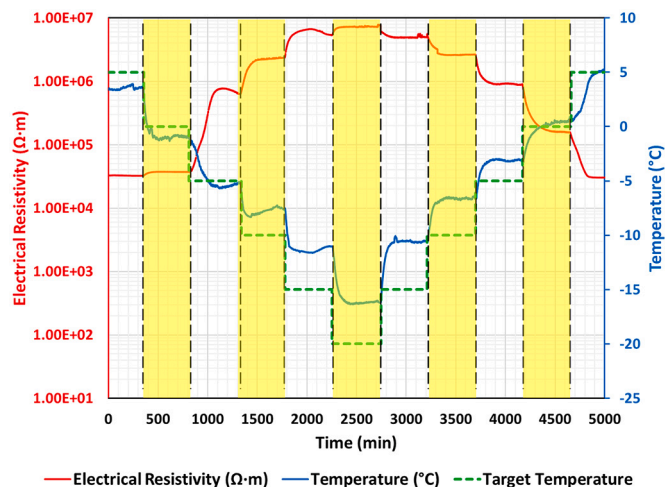**Fig. 2.** Temperature path for a full freeze–thaw cycle.

Fig. 3. Evolution of electrical resistivity with temperature in test period (for Test Set No. 5, with water content of 11% and bulk density of 1.85 g/cm³).

3. Experimental characterization

3.1. Materials

To investigate the correlation between temperature and soil electrical resistivity, we carried out a number of experimental tests using clayey sand. According to Federal Highway Administration (FHWA (2010)) specifications, this soil can be classified as frost–susceptible, as it contains 19% (by weight) of fine particles that are smaller than 0.02 mm. The basic physical properties of the soil are shown in Table 3. It belongs to clayey sand (SC) based on the Unified Soil Classification System (USCS). The clayey sand used in this study was obtained from a local contractor in New Jersey. Soil samples were oven-dried and crushed before the experiments to minimize the presence of large clumps.

3.2. Experimental setup and testing procedure

Fig. 1 provides an overall view of the experimental setup. The soil samples were tested in an enclosed container that provided a transmission path for the electric current and minimized the evaporative water loss during the test. To achieve this, a soil sample holder was designed and fabricated using an acrylic cylinder, stainless steel (SS) plate electrodes (current injection ends), SS rod electrodes (voltage measurement), and apparatus closure and sealing materials. Soil samples were prepared by homogeneously mixing dry soils with the initial water content followed by compaction in multiple layers to reach the target bulk density. Table 4 summarizes the initial water content and bulk density values of the test samples. The frost susceptibility level of the soil was determined to be medium following the United States Army Corps of Engineers Engineering Manual USACE EM 1110–3-138 (1984). For each test run, samples of desired initial water contents were prepared by mixing dry soil with distilled water, and samples of desired bulk density were achieved using the layered compaction method in the acrylic cylinder. The experimental setup was validated as repeatable electrical resistivity results were obtained (with a set of 3 soil specimen with the same properties and temperature conditions, coefficient of variation <10%).

Each soil column was instrumented with four electrodes (two current excitation, two voltage detection) and a thermocouple mounted in the center. The soil columns were placed inside an environmental chamber (Controls Group, USA) with all connecting wires passed through an access port to the external measurement systems. Temperature data were sent to a PC through a data logger and Wi–Fi modem. Resistance data acquired by a Miller 400D (M.C.Miller, USA) were transmitted to the PC through Bluetooth. Resistivity values were calculated from the following equation:

$$\rho = R\frac{A}{a} \tag{1}$$

where ρ represents electrical resistivity (Ω•m), R represents resistance (Ω), A represents cross sectional area of the soil column (m²), and a represents inner electrode spacing (m).

To enable the simultaneous measurement of multiple soil columns, a multi-switch was designed and integrated into the electrical resistivity measurement system. The sampling frequencies for electrical resistivity and temperature were set to one data point per minute. To simulate a full freeze–thaw cycle of 5 °C to −20 °C, then back to 5 °C, the chamber temperature was scheduled to change 5 °C every 8 h (Fig. 2). The interval of 8 h, selected based on preliminary tests, is to ensure that the soil electrical resistivity reached its stabilized value during each temperature interval.

parameters, such as those related to soil microstructure, may require complicated measuring processes, which are difficult to calibrate. Some other models, such as those of Wu et al. (2017) and (Briggs et al., 2017) were developed based on the empirical correlation between electrical resistivity and temperature. The models developed by Wu et al. (2017), Herring et al. (2019), and (Briggs et al., 2017) are only applicable for subzero temperatures. The models developed by Ming et al. (2020), Shan et al. (2017), and Tang et al. (2018) require pore diameter distribution or unfrozen water content as inputs, which are difficult to obtain under laboratory conditions. Generally, most resistivity models from past studies are either limited to monotonic temperature variations within a narrow range, or require specialized equipment to acquire input parameter values. As an alternative, Lyu et al. (2019) developed a sigmoidal function to correlate resistivity with temperature, which could be easily inferred from experiments. Beyond good data fitting, a sigmoidal function that contains a maximum, a minimum, and a rapid transition zone is suitable to reveal the change in unfrozen water content of soil during freezing and thawing, which is the main cause of variance in electrical resistivity. This informed the approach adopted in our study, where electrical resistivity was correlated with temperature in a sigmoidal function for soil samples with different properties, as well as the freezing stage and the thawing stage.
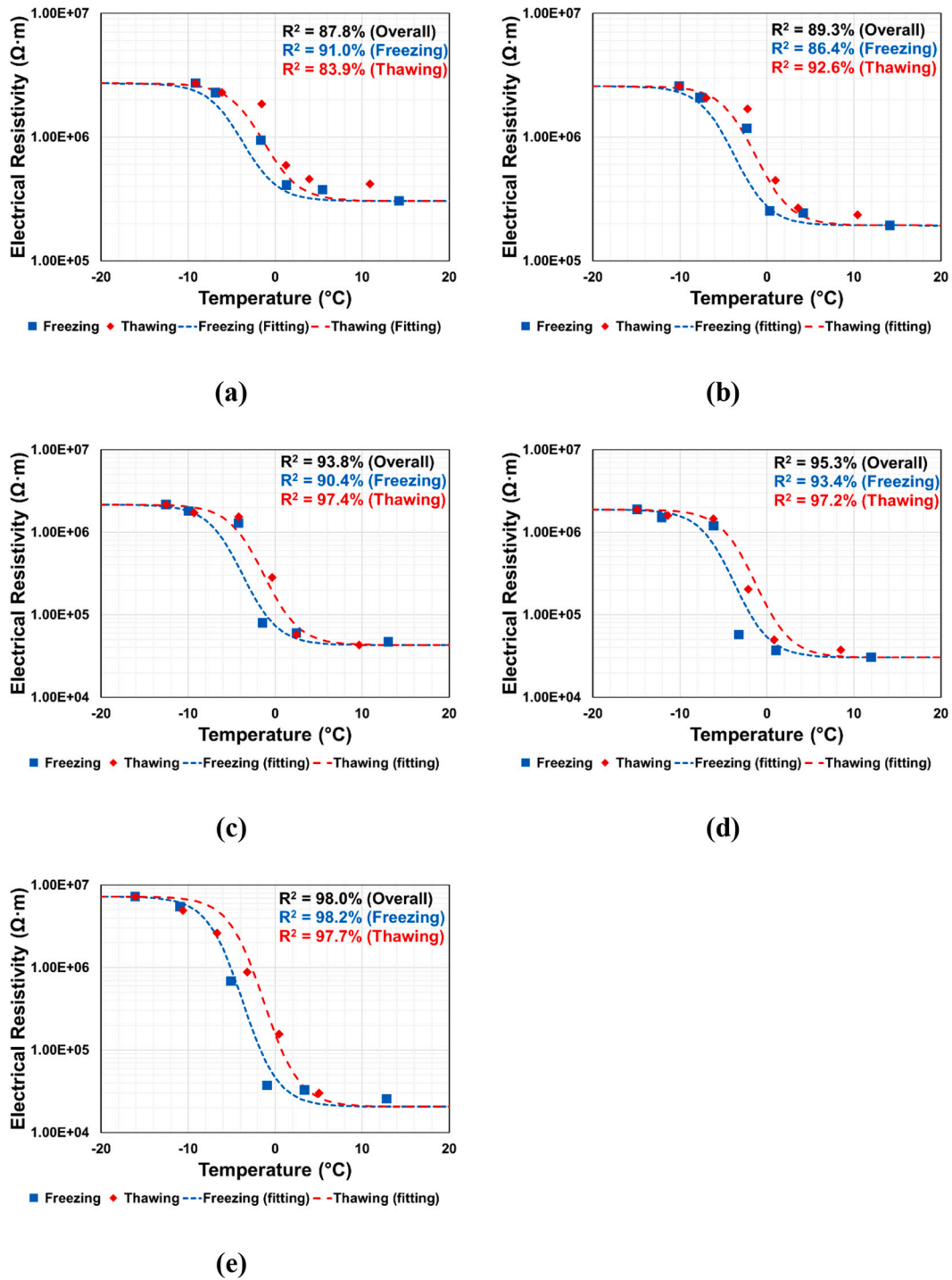
Fig. 4. Parameter fitting of electrical resistivity: (a) initial water content = 6.5%, bulk density = 1.65 g/cm^3; (b) initial water content = 7.5%, bulk density = 1.75 g/cm^3; (c) initial water content = 11%, bulk density = 1.85 g/cm^3 (d) initial water content = 15%, bulk density = 1.75 g/cm^3; (e) initial water content = 16.5%, bulk density = 1.65 g/cm^3.

3.3. Temporal evolution of soil electrical resistivity under sub–freezing conditions

The general trend showed electrical resistivity to be negatively correlated with temperature. That is, the lower the temperature, the higher the electrical resistivity value. Fig. 3 shows the temporal change of temperature and electrical resistivity for one sample (water content is 16.5% and bulk density is 1.65 g/cm^3) in the test scheme. The soil temperature profile followed the designed chamber temperature path

with deviations. Another phenomenon to note is that the increment of electrical resistivity increased from around 10^5 Ω·m to around 10^6 Ω·m when target temperature decreased from 0 °C to −10 °C, while the change was from 10^6 Ω·m to 10^7 Ω·m when target temperature decreased from −10 °C to −20 °C. When soil column temperature stabilized, the soil electrical resistivity value also stabilized, which was taken as the electrical resistivity value for that specific temperature level. Similar trends were obtained for the other tested samples. This dependence of soil electrical resistivity on temperature was dominated
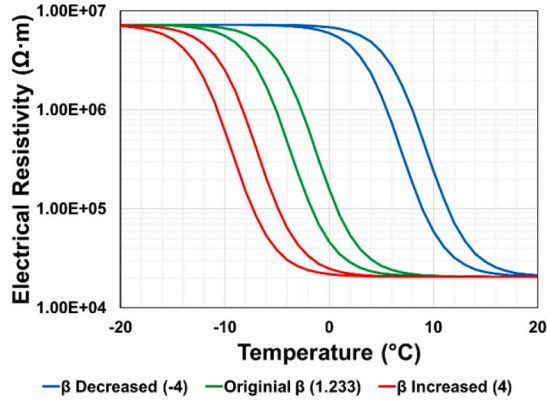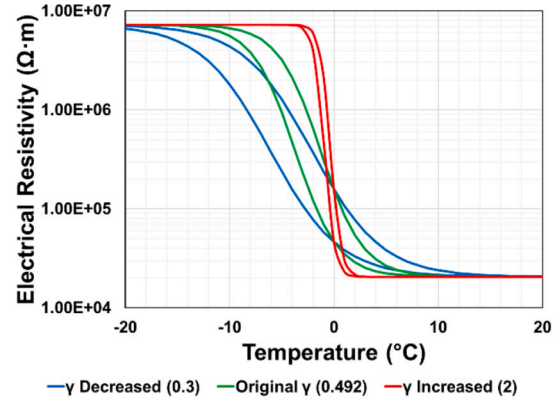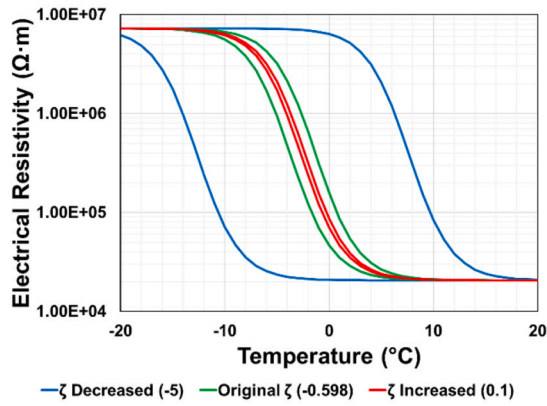
Fig. 5. Influence of parameters β, γ, and ζ on fitting curves: (a) changing β values; (b) changing γ values; (c) changing ζ values. (The original curve is from the fitted function for Test Set No.5).

Table 2
Calibrated and validated parameter values for the sigmoidal model.

Parameter	Value
δ	5.483 (No. 1)
	5.286 (No. 2)
	4.633 (No. 3)
	4.481 (No. 4)
	4.314 (No. 5)
α	0.951 (No. 1)
	1.125 (No. 2)
	1.701 (No. 3)
	1.794 (No. 4)
	2.546 (No. 5)
$S(\zeta)$	0.598 (freezing)
	−0.598 (thawing)
β	1.233
γ	0.492

Table 3
Basic properties of the soil sample.

Properties	Values
Optimum water content w_{op} (%)	11.4
Maximum dry density ρ_d (g·cm^{-3})	1.9
Plastic limit (PL)	17.7
Liquid limit (LL)	25.93
Plasticity index (IP)	8.23
Void Ratio (e)	0.59
Specific gravity (Gs)	2.63
Dominant minerals	Quartz and Gismondine
Soil classification	SC (Clayey Sand)
Frost susceptibility level	Medium

Table 4
Water content and bulk density values of tested soil samples.

Test Set	Water Content (%)	Bulk density (g/cm^3)
1	6.5	1.65
2	7.5	1.75
3	11	1.85
4	15	1.75
5	16.5	1.65

by the water–ice phase change within the soil body. Ice has a much higher electrical resistivity than water (10^7–10^8 Ω·m for ice compared to 10^0–10^2 Ω·m for potable water (Petrenko, 1993)). As unfrozen pore water gradually changed to ice under freezing temperatures, the overall soil electrical resistivity experienced a large increase. Additionally, the increment of electrical resistivity was from around 10^5 Ω·m to around 10^6 Ω·m when temperature decreased from 0 °C to −10 °C, while the
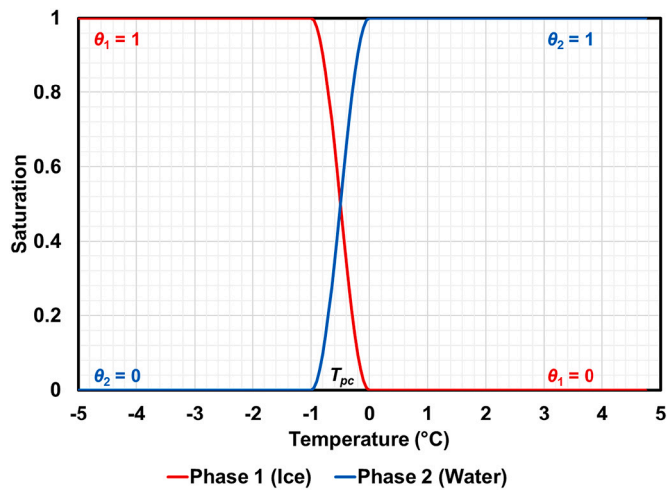
Fig. 6. Schematic view of temperature-dependent ice-water phase change process. (θ_1 and θ_2 are degree of saturation for ice and water, respectively; T_{pc} is the freezing and melting temperature set in the model).

Table 5
Material input parameters for the COMSOL numerical model.

Material	Property	Value	Reference
Soil Solids	Thermal conductivity	5.85 W/(m·K)	(Chesworth, 2007)
	Density	2625 kg/m^3	(Chesworth, 2007)
	Heat capacity	835 J/(kg·K)	(Chesworth, 2007)
	Electrical conductivity	ρ^{-1} (S/m)	This study
	Relative permittivity	6.5	(Knight and Endres, 2005)
	Void ratio	0.59	This study
	Specific gravity	2.63	This study
Water	Thermal conductivity	0.6 W/(m·K)	(Young et al., 1996)
	Density	1000 kg/m^3	(Young et al., 1996)
	Heat capacity	4187 J/(kg·K)	(Young et al., 1996)
Ice	Thermal conductivity	1.6 W/(m·K)	(Young et al., 1996)
	Density	920 kg/m^3	(Young et al., 1996)
	Heat capacity	2108 J/(kg·K)	(Young et al., 1996)

increment was between 10^6 Ω·m and 10^7 Ω·m when the temperature decreases from −10 °C to −20 °C. This was attributed to the fact that most pore water transformed into ice during the first 0 °C to −10 °C interval, leaving much less pore water in the unfrozen state to freeze in the temperature regime below −10 °C. Studies the soil freezing characteristic curve, such as Bai et al. (2018), also show that a larger amount of unfrozen water content is reduced when temperature drops from 0 °C to −10 °C than that when temperature drops from −10 °C to −20 °C. This is because bulk water and capillary water consist most of the unfrozen water of the soil, and are transformed into ice first during the freezing process; meanwhile, bound water consists only a small portion of unfrozen water, but requires more energy to be transformed into ice (Chai et al., 2018). The patterns of electrical resistivity change and unfrozen water content change with temperature are similar due to the strong correlation of the two based on Archie's Law (Archie, 1942).

3.4. Hysteresis response of soil electrical resistivity under sub–freezing conditions

Experimental results indicate that the electrical resistivity increased nonlinearly with the decreasing temperature (Fig. 4). The soil electrical resistivity was most sensitive to temperature variation in the range of −10 °C to 0 °C. More importantly, hysteresis in electrical resistivity were observed when comparing the freezing and thawing paths, as reflected by the blue and red dots in Fig. 4. Electrical resistivity obtained from the thawing path was typically higher than the resistivity obtained from the

freezing path at the same temperature. Similar hysteresis phenomenon was observed in other researchers' studies as well. Slater and Glaser (2003) observed a hysteresis response between electrical resistivity and water saturation levels for sandy soil. Interpreting our results using the concept of saturation, we can conclude that the liquid water saturation for electrical conduction was reduced with the increasing ice content as temperature decreases under sub-freezing conditions. Tian et al. (2014) described hysteresis effects between unfrozen water content and temperature in artificial clay-sand mixtures using the nuclear magnetic resonance (NMR) technique, and found that the unfrozen water content during the freezing stage was generally higher than that during the thawing stage between −6 °C and − 2 °C. Kang and Lee (2015) reported that the electrical resistivity of sand–silt mixtures (40% saturation) during thawing was lower than that during freezing, which might be contributed by the formation of unfrozen water film along the soil particles during thawing. Wu et al. (2017) showed consistently lower electrical resistivity during freezing compared to that during thawing in natural permafrost, and suggested that the resistivity shift might reflect changes in the distribution pattern of the unfrozen water in the soil matrix. Additionally, field measurements in the Alpine Region by Supper et al. (2014) showed a similar hysteresis phenomenon with lowered resistivity during freezing. However, as summarized in Table 1, previous models are not suited for capturing hysteresis phenomena, highlighting the need for a new theoretical electrical resistivity model.

To account for the S–shaped evolution of soil electrical resistivity under the freeze–thaw cycle, we adopted a sigmoidal function to fit the experimental data:

$$log\rho = \delta + \frac{\alpha}{1 + e^{\beta + S(\zeta) + \gamma T}} \quad (2)$$

where ρ is electrical resistivity (Ω·m), δ is the lower bound of electrical resistivity, $\delta + \alpha$ is the upper bound of electrical resistivity, T is temperature (°C), S(ζ) is a state variable (S = −1 when freezing, S = 1 when thawing), and β, ζ, and γ are fitting parameters (assigned as constants for all samples). To better understand the physical meaning of the fitting parameters β, γ, and ζ, we first carried out a sensitivity analysis. Sensitivity analysis results (Fig. 5) showed the influence of these parameters on the soil electrical resistivity. Increasing β decreased the soil electrical resistivity during both freezing and thawing stages, which indicates that β may be related to the concentration of solute in pore fluid of soil. Increasing γ accelerated the temperature-dependent variation of the electrical resistivity, and reduced the hysteresis phenomenon as reflected by the closer curves during freezing and thawing, which indicates that γ may be related to the amount of unfrozen water change. Creasing ζ significantly reduced the hysteresis phenomenon while maintaining the rate of electrical resistivity change, which indicates that ζ may be related to irreversible soil structure change.

In this model, the lower and upper bounds (δ and $\delta + \alpha$) correspond to the resistivity values of a soil sample at maximum measured temperature (approximately room temperature) and the measured minimum temperature (approximately from −20 °C to −10 °C) during the tests, respectively. We assume that the minimum and maximum values of electrical resistivity obtained from experiments can be used to approximate the lower and upper bounds. Based on experimental data, we applied the nonlinear generalized reduced gradient (GRG) method to maximize the coefficients of determination (R^2) values for the fitted curve, with the R^2 value calculated as:

$$R^2 = 1 - \left[\sum_i (y_i - f_i)^2 \right] \Big/ \left[\sum_i (y_i - \bar{y})^2 \right] \quad (3)$$

where R^2 is the coefficient of determination; y_i is experimental data at a certain temperature; f_i is modeled data at the same temperature; and $\bar{y}$ is the average of the experimental data. Note that out of all five samples, four were used to calibrate S (ζ), β and γ values. From optimization results, we can summarize the parameter values in Table 2. After

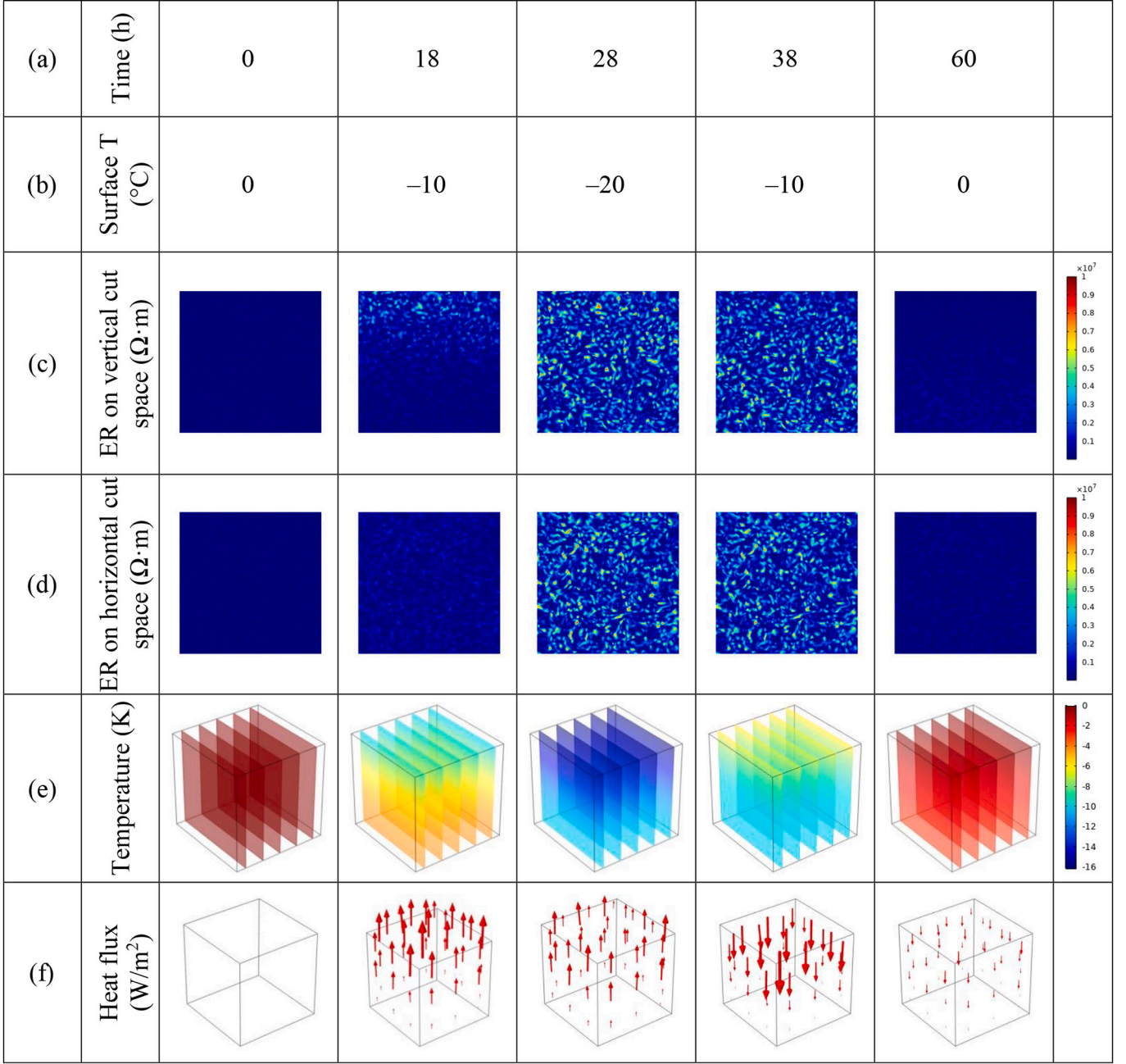| (a)	Time (h)	0	18	28	38	60	
(b)	Surface T (°C)	0	−10	−20	−10	0	
(c)	ER on vertical cut space (Ω·m)						
(d)	ER on horizontal cut space (Ω·m)						
(e)	Temperature (K)						
(f)	Heat flux (W/m²)						

Fig. 7. Spatiotemporal evolution of electrical resistivity (ER), temperature (T), and heat flux in the cubic space (5 slices inside the cube are shown for demonstration purpose).

calibration, the fifth sample (initial water content = 16.5%, bulk density = 1.65 g/cm³) was used for validation purpose. The dashed lines in Fig. 4 show that the input parameters determined above were able to fit the experimental data of all samples under varying conditions with R^2 consistently above 80%. This sigmoidal function-based model was able to capture the hysteresis response of soil electrical resistivity under the freeze-thaw process, and can be applied to predict soil electrical resistivity under a more general thermal environment (as discussed in the following section).

4. Numerical simulation

4.1. Governing equations

To overcome the limitations of existing electrical resistivity models

as summarized in Section 2, we used the sigmoidal function deduced from experimental observations as a basis to build a numerical model. In this study, we developed a finite element model to investigate the electrical resistivity evolution of frozen ground considering the influence of soil depth and atmospheric temperature conditions. This clayey sand in the model adopts the same properties as the soil tested in our physical experiments. The formulated multiphysics coupled model accounts for electrical resistivity evolution, soil thermal responses, and phase changes. Summarized below are the major governing equations.

The heat transfer in the porous medium is governed by the following equation:

$$(\rho_d C)_{eq}\frac{\partial T}{\partial t} + \rho C_w u \bullet \nabla T + \nabla \bullet \left(-k_{eq}\nabla T \right) = Q \tag{4}$$

where $(\rho_d C)_{eq}$ is the equivalent value of density ρ_d (kg/m³) and heat
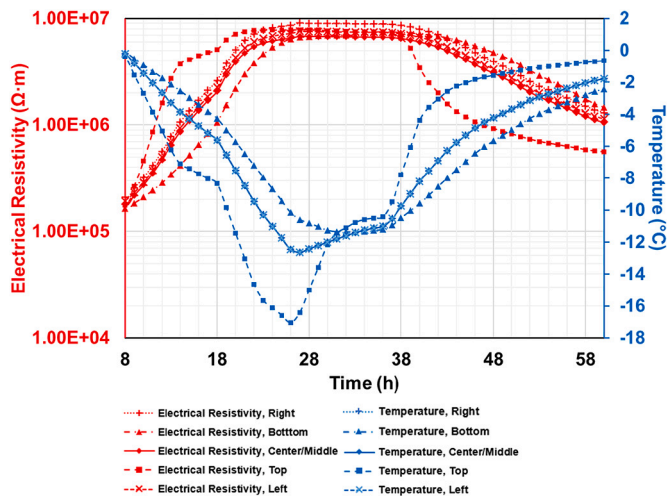
8

Fig. 8. Evolution of electrical resistivity and temperature with respect to time at different locations inside the cubic space (center/middle point is located at the center of the cube; top, bottom, left, right are points close to top, bottom, left, and right boundaries, with a 5–cm gap, respectively).

Fig. 9. Relationship between electrical resistivity versus temperature at different locations inside the cubic space (center/middle point is located at the center of the cube; top, bottom, left, right are points close to top, bottom, left, and right boundaries with a 5–cm gap, respectively).
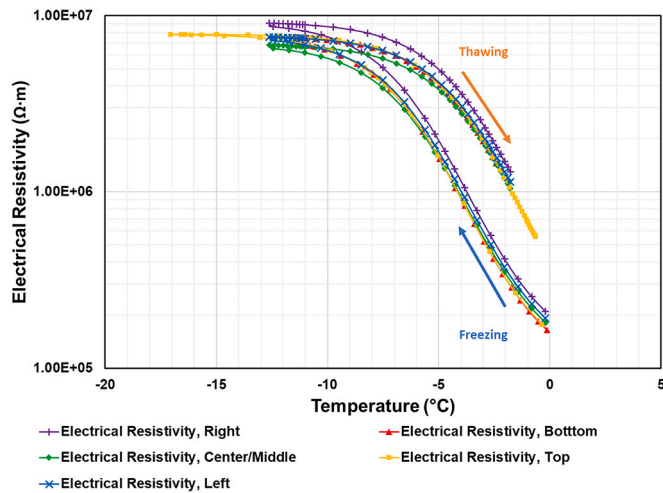
capacity C (J/kg·K) at constant pressure of the porous media, k_{eq} is the effective thermal conductivity (W/m·K) of the porous media, T is the temperature (K), Q is a heat flux (W/m^3), and C_w is the effective fluid's heat capacity at constant pressure.

Fig. 6 shows the transition process between water and ice phases under temperature variations. The liquid water saturation S_w depends on the phase change process as:

$$S_w = S_{unf} + (1 - S_{unf})\theta_2 \qquad (5)$$

where S_{unf} is the unfrozen water saturation, assumed to be 0.05 from averaged estimated values by Herring et al. (2019). It should be noted that the actual unfrozen water content can be larger than the one in the model due to the existence of bound water other than bulk water capillary water, and the actual unfrozen water content varies with temperature. $\theta_2(T)$ is the smooth step function ($\theta_2(T) = 0$ for temperatures below the melting temperature T_{pc}, and $\theta_2(T) = 1$ for temperatures above T_{pc}). In this study, it is assumed that the transition zone extends

from 0 to −1 °C, and T_{pc} is set to be −0.5 °C. It should be noted that the actual transition zone may have a different temperature range, depending on the measurement of unfrozen water content. Therefore, our model sets liquid water saturation S_w as temperature-dependent, and unfrozen water saturation S_{unf} as a constant (temperature-independent).

The evolution of soil electrical resistivity was governed by Eq. (2) (as described in Section 3.4). These equations summarized above were implemented in COMSOL Multiphysics 5.5 for the assessment of soil electrical resistivity under two scenarios: (1) heterogeneous soil at Representative Elementary Volume (REV) scale under short–term thermal variations; and (2) field–scale soil under long–term natural atmospheric temperature variations.

4.2. REV-scale model

4.2.1. Model configuration

To account for the soil property heterogeneity, we developed a random finite element model in COMSOL. In this model, a 3D cubic soil domain was created, with an equal side dimension of 30 cm. The entire domain was meshed into 16,300 tetrahedral elements, with each element having a volume of 0.027 m^3. Four side boundaries and bottom surface were thermal–insulated, while the top boundary was subjected to the similar staged freeze–thaw temperature path as shown in Fig. 2. More specifically, the target temperature decreased from 0 to −20 °C, and then increased from –20 °C to 0 °C with a 10 °C level in 48 h. The final temperature interval at 0 °C was extended by an additional 12 h to reach the target temperature due to the gradual transfer of heat in the soil body. This model was designed to simulate the influence of freeze-thaw thermal variations on soil grounds. To create the heterogeneous soil structure, random values were assigned to the sigmoidal model parameters δ and α at varying locations (i.e. elements) of the cube. According to results from Section 3.4, we set upper and lower bounds of δ to be 5.483 and 4.314, respectively; and upper and lower bounds of α to be 2.546 and 0.951, respectively. Table 5 summarizes material input parameters for the COMSOL numerical model.

4.2.2. Influence of short–term temperature change (REV-scale model)

After the simulation of the staged target thermal path between 0 °C and 20 °C, we plotted the evolution process of soil electrical resistivity (see Fig. 7). An inhomogeneous distribution of electrical resistivity can be observed in the cubic space, attributed to the randomly distributed soil properties. The contour plots of the two cut planes (both passing through the central point of the cube) along the vertical and horizontal directions further validate the heterogeneous soil response (Fig. 7c, d). From 0 h to 28 h, the cubic space was generally cooling, resulting in a gradual increment of the soil electrical resistivity. From 28 h to 60 h, the cubic space was generally warming, so there was a gradual decrease in electrical resistivity. At $t = 18$ h, the upper soil layers showed a clear increase of electrical resistivity first (Fig. 7c), whereas the bottom resistivity remains low due to the higher local temperature. Since the heat transfer is along the vertical direction (Fig. 7e, f), the soil electrical resistivity within the horizontal plane changes simultaneously (Fig. 7d).

We also plotted the temporal variations of electrical resistivity and temperature changes for 5 observation points (Fig. 8), with one at the center of the cube and the other four close to the top, bottom, left, and right boundaries (top, center, bottom points are in the same vertical cut plane; and left, center, right points are in the same horizontal cut plane), respectively. Due to the gradual heat transfer process, trends in temperature showed that locations close to the top boundary were most sensitive to surface temperature change, whereas locations close to the bottom boundary were least sensitive. Therefore, when atmospheric temperature decreased on the surface, the top point showed more rapid electrical resistivity changes with time than the other points, as reflected by the largest slope within 8– 18 h. A similar, but opposite, trend existed when temperature increased (within 38–48 h). The electrical resistivity
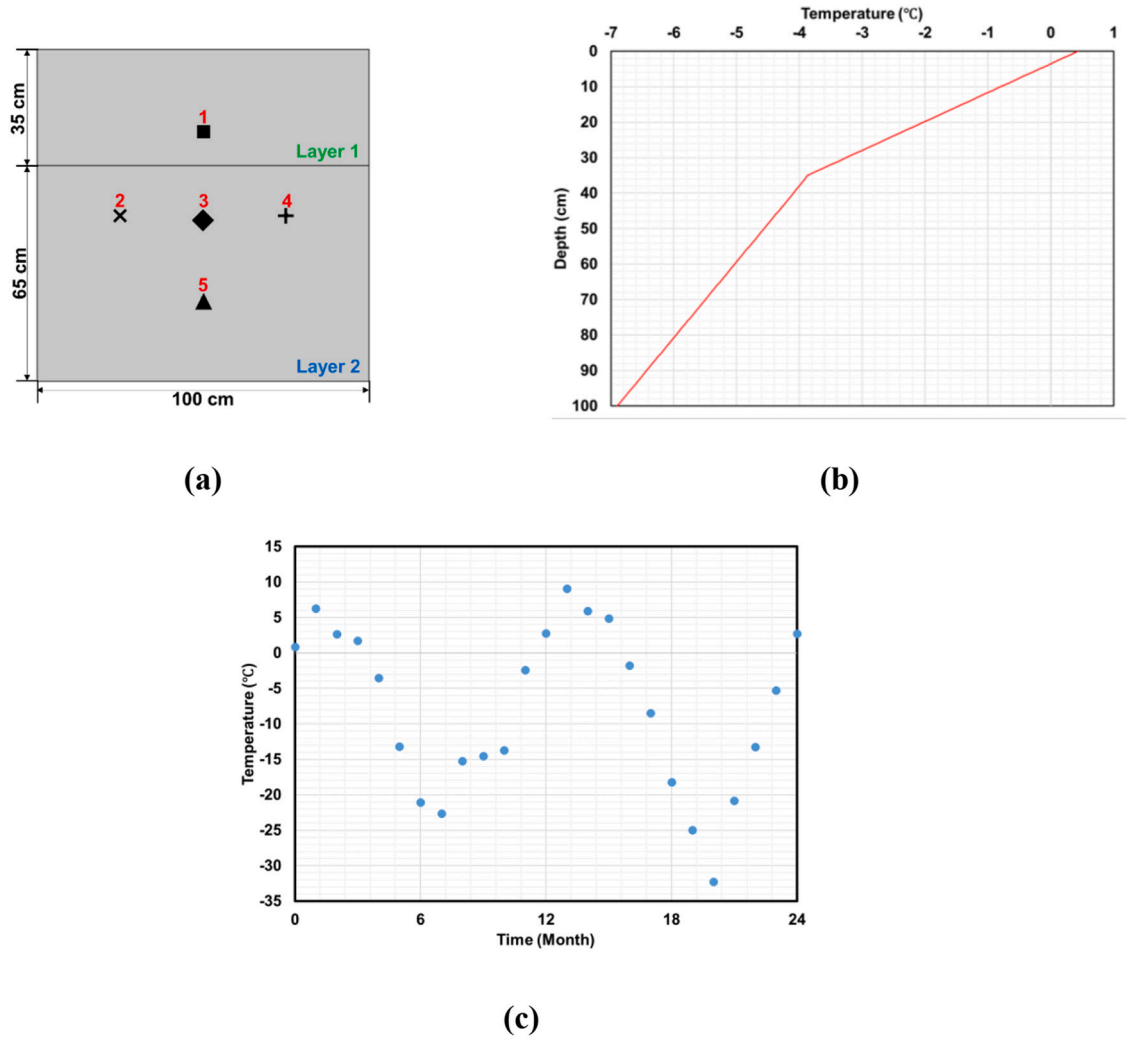
Fig. 10. (a) field-scale model geometry; (b) initial soil temperature conditions; and (c) atmospheric temperature of 2-year period (from June 2018 to June 2020, 24 months).

measured at all points reached stabilization during the constant temperature interval. The stabilized value depended on both local temperature and local soil properties. Under freezing, because the bottom was warmer, the local unfrozen water content was higher, resulting in the lowest electrical resistivity at the bottom point than other points. Also, the slightly different electrical resistivity values recorded at left, right and middle points (same horizontal plane) highlight the impact of soil homogeneity. Fig. 9 presents the correlations between electrical conductivity and temperature at five points. All of them follow the designated hysteresis electrical resistivity behavior. Three points on the same horizontal plane showed a similar response, with slight differences caused by the local property heterogeneity. The bottom point had a consistently higher conductivity since the temperature variation at the bottom is smaller in comparison to that at the surface boundary or shallower depth. This simulation further highlights the important role of both temperature and soil property in governing the electrical response of soils.

4.3. Field scale-model

4.3.1. Model configuration

Based on the field condition at Utiqiagvik (formerly Barrow), Alaska as described by Hinkel et al. (2001). In the described site, the main type of soil was estimated to be saturated, fine-grained mixed mineral soils.

(Hinkel et al., 2001).We considered two layers (the upper layer with 35-cm thickness and the lower layer with 65-cm thickness) in the 2D field–scale model (Fig. 10b). Initial temperature of the two layers varied with depth, with a relatively higher temperature profile for the upper layer to simulate the active layer in cold regions. Water saturation under unfrozen conditions was 100%, corresponding to an initial water content of 22.4%. Additionally, five observations points were selected in the soil to monitor the spatiotemporal changes of soil properties (Fig. 10a). They were located at the center of the 100–cm–by–100–cm geometry, with a spacing of 25 cm. The top boundary of the modeled region followed the air temperature changes, the left, right, and bottom side boundaries were thermally insulated. The entire model geometry was then meshed into 1924 triangular elements, with the element size of 5.2 $\times$ 10^{-4} m^2. The air temperature change within two-year period (from June 2018 to June 2020) was obtained from historical data of monthly averaged air temperature at Utiqiagvik (formerly Barrow), Alaska. The air temperature reached the maximum value of 6.3 °C in July 2018 and 9.1 °C in July 2019, and reached the minimum value of -22.6 °C in January 2019 and -32.3 °C in February 2020 (Fig. 10c).

From the observations by Hinkel et al. (2001), we set the initial temperature of Layer 1 and Layer 2 as a function of depth (Fig. 10):

$$T_{ini} = \begin{cases} -0.123d + 0.4314, d \leq 35 \\ -0.0467d - 2.2291, d > 35 \end{cases} \qquad (6)$$
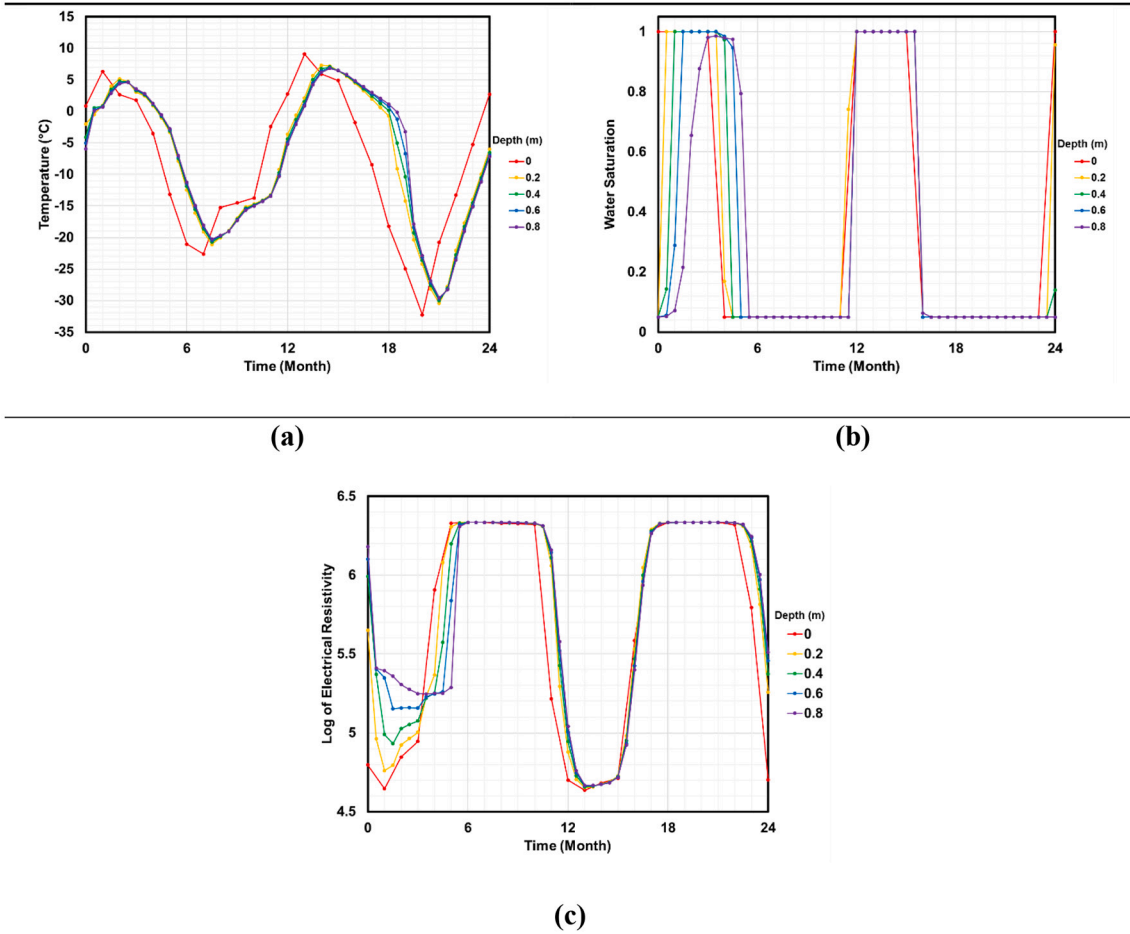
Fig. 11. Long-term (2-year) simulation of field-scale model: (a) temperature; (b) water saturation; and (c) electrical resistivity.

where T_{ini} (°C) is the soil initial temperature, d (cm) is depth. Then, surface temperature change for the long–term followed the local field–monitored atmospheric temperature in two years (June 2018 to June 2020, from NOAA (2019)).

4.3.2. Influence of long–term temperature change (field-scale model)

Fig. 11 presents the spatiotemporal evolution of soil temperature (Fig. 11a), ice–water phase transition (Fig. 11b), and the electrical resistivity of the ground (Fig. 11c) within the two–year period. In Fig. 11a, temperature of soil at different depths reached peaks in July 2018 (Month 1) and July 2019 (Month 13), and valleys in January 2019 (Month 7) and February 2020 (Month 20), consistent with the atmospheric temperature variations. The shallow region was closer to air, so it led the changes in temperature, whereas the deeper region presented slightly delayed temperature changes. As soil temperature increased, the degree of saturation increased and reached 1 when soil temperature is above 0 °C. In the meantime, due to the increasing amount of unfrozen water, soil electrical resistivity decreased. On the other hand, when soil temperature decreased to its minimum, water saturation decreases to 0.05 (only residual unfrozen water exists), and electrical resistivity reached its maximum. These results indicate that the change of an environmental factor, such as air temperature at the site of interest, strongly impact soil temperature at different depths, thereby influencing water saturation and electrical resistivity of soil.

To better illustrate the spatiotemporal changes of parameters, we made contour plots for simulation results in a two–year period (Fig. 12). We can see from Fig. 12a that soil temperatures were mostly above 0 °C between June 2018 and December 2018, and between Jun 2019 and December 2019. Again, the result revealed that temporal changes in soil

temperature were slower than those in air temperature. Similarly, in Fig. 12b, we can see that water saturation was mostly 100% (unfrozen state of soil) between June 2018 and December 2018. Therefore, we can see relatively lower electrical resistivity between June 2018 and December 2018 in Fig. 12c.

Although the COMSOL simulation can be used to forecast the results of geophysical investigation in cold regions, we may still encounter several challenges, including soil cracking, air voids, and complex correlations between electrical data and soil properties. It should be noted that there are still other influencing factors of soil on electrical resistivity not discussed in this study, including concentration of solutes in the pore fluid, grain size distribution, and soil mineralogy. As for the future work, we are planning to set salt concentration in the soil pore fluid as one of the testing parameters, investigate resistivity changes in a wider temperature region, and compare the results obtained from both electrical and electromagnetic methods.

5. Conclusion

This study investigates the electrical resistivity of clayey soils under thawed and freezing conditions. By conducting laboratory experiments using the Wenner four–electrode method, we developed a sigmoidal model to fit the electrical resistivity hysteresis response of the frozen soil. Finite element implementation of models with both short–term and long–term temperature variations enabled us to simulate the heat transfer and electrical response of heterogeneous soils at different scales. The main conclusions of our research are:
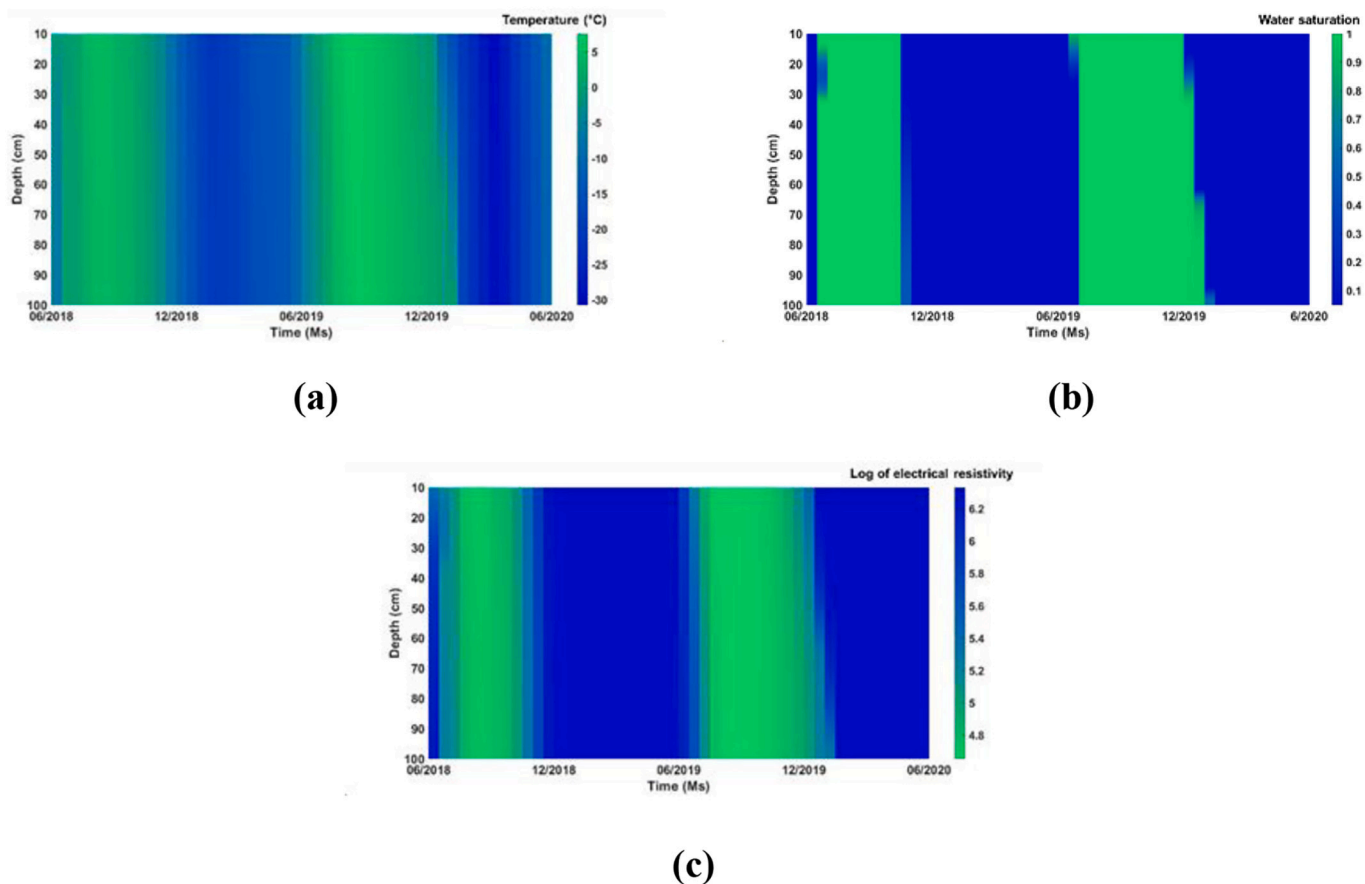
Fig. 12. Contour plots of parameters distribution in the simulated 2-year period: (a) temperature; (b) water saturation; and (c) electrical resistivity.

- Below 0 °C, soil resistivity increases with the decreasing temperature. There also exists an electrical resistivity hysteresis phenomenon for the soils tested under freeze–thaw temperature variations. Based on the soils tested in this study, at the same temperature, electrical resistivity during freezing is consistently lower than that during thawing.
- A sigmoidal model has been developed to fit experimental data and capture the hysteresis phenomenon. The model uses soil temperature and moisture content-dependent material properties as inputs. Implementation of the sigmoidal model into the finite element model helps capture the irreversible physical changes in soil under freeze–thaw cycles.
- Changes of atmospheric temperature in short–term and long–term periods lead to soil temperature change, and thereby phase transition in the pore fluid between ice and water, and electrical resistivity change. The timing of these processes depends on the depth and soil properties, including initial water content and temperature.

This study provides new insights into the fundamental mechanisms that govern the electrical behaviors of frozen soils and will help improve the future application of electrical geophysical investigations in cold regions.

CRediT authorship contribution statement

Rui Liu: Methodology, Formal analysis, Investigation, Data curation, Writing – original draft. **Cheng Zhu:** Methodology, Writing – review & editing, Supervision, Funding acquisition. **John Schmalzel:** Methodology, Resources, Writing – review & editing. **Daniel Offenbacker:** Methodology, Formal analysis. **Yusuf Mehta:** Supervision, Funding acquisition. **Benjamin Barrowes:** Methodology, Formal analysis, Writing – review & editing. **Danney Glaser:** Methodology, Formal analysis, Writing – review & editing. **Wade Lein:** Project administration.

Declaration of Competing Interest

The authors declare that they have no known competing financial interests or personal relationships that could have appeared to influence the work reported in this paper.

References

Ahmed, A., Hossain, M.D.S., Khan, M.S., Greenwood, K., Shishani, A., 2017. Moisture Variation in Expansive Subgrade through Field Instrumentation and Geophysical Testing. Springer, pp. 45–58.

Archie, G.E., 1942. The electrical resistivity log as an aid in determining some reservoir characteristics. Trans. Am. Inst. Mech. Eng. 146, 54–67.

AzariJafari, H., Yahia, A., Amor, B., 2018. Assessing the individual and combined effects of uncertainty and variability sources in comparative LCA of pavements. Int. J. Life Cycle Assess. 23, 1888–1902.

Bai, R.Q., Lai, Y.M., Zhang, M.Y., Yu, F., 2018. Theory and application of a novel soil freezing characteristic curve. Appl. Therm. Eng. 129, 1106–1114.

Briggs, M.A., Campbell, S., Nolan, J., Walvoord, M.A., Ntarlagiannis, D., Day-Lewis, F.D., Lane, J.W., 2017. Surface geophysical methods for characterising frozen ground in transitional permafrost landscapes. Permafr. Periglac. Process. 28, 52–65.

Chai, M., Zhang, J., Zhang, H., Mu, Y., Sun, G., Yin, Z.J.A.C.S., 2018. A method for calculating unfrozen water content of silty clay with consideration of freezing point. Appl. Clay Sci. 161, 474–481.

Chapman, W.L., Walsh, J.E., 2007. Simulations of Arctic temperature and pressure by global coupled models. J. Clim. 20, 609–632.

Chesworth, W., 2007. Encyclopedia of Soil Science. Springer Science & Business Media.

FHWA, 2010. Geotechnical Aspects of Pavements: Reference Manual. US Department of Transportation, Federal Highway Administration.

Gan, J., Zhang, Y.X., Liu, X., 2020. An application of the high-density electrical resistivity method for detecting slide zones in deep-seated landslides in limestone areas. J. Appl. Geophys. 177, 1–13, 104013.

Gance, J., Malet, J.P., Supper, R., Sailhac, P., Ottowitz, D., Jochum, B., 2016. Permanent electrical resistivity measurements for monitoring water circulation in clayey landslides. J. Appl. Geophys. 126, 98–115.

Glaser, D., Rucker, D., McGill, R., Fink, J., Baldyga, C., Hansen, J., Magliocchino, A., 2005. Residual Potential Mapping of Contaminant Transport Pathways in Karst Formations of Southern Texas, Sinkholes and the Engineering and Environmental Impacts of Karst, pp. 590–597.

Glover, P.W.J., 2010. A generalized Archie's law for n phases. Geophysics 75, E247–E265.

Glover, P.W.J., 2017. A new theoretical interpretation of Archie's saturation exponent. Solid Earth 8, 805–816.

Han, T.-C., Yan, H., Fu, L.-Y., 2021. A quantitative interpretation of the saturation exponent in Archie's equations. Pet. Sci. 18, 444–449.

Harris, S.A., 2018. Geocryology : Characteristics and Use of Frozen Ground and Permafrost Landforms, 1st edn. CRC Press/Balkema is an imprint of the Taylor & Francis Group, Boca Raton, Florida.

Hauck, C., 2002. Frozen ground monitoring using DC resistivity tomography. Geophys. Res. Lett. 29, 12-11–12-14.

Herring, T., Cey, E., Pidlisecky, A., 2019. Electrical resistivity of a partially saturated porous medium at subzero temperatures. Vadose Zone J. 18.

Hinkel, K.M., Paetzold, F., Nelson, F.E., Bockheim, J.G., 2001. Patterns of soil temperature and moisture in the active layer and upper permafrost at Barrow, Alaska: 1993–1999. Glob. Planet. Chang. 29, 293–309.

Hong, E., Perkins, R., Trainor, S., 2014. Thaw settlement hazard of permafrost related to climate warming in Alaska. ARCTIC 67, 93–103.

Kang, M., Lee, J.S., 2015. Evaluation of the freezing–thawing effect in sand–silt mixtures using elastic waves and electrical resistivity. Cold Reg. Sci. Technol. 113, 1–11.

Kneisel, C., Hauck, C., Fortier, R., Moorman, B., 2008. Advances in geophysical methods for permafrost investigations. Permafr. Periglac. Process. 19, 157–178.

Knight, R.J., Endres, A.L., 2005. An introduction to rock physics principles for near-surface geophysics, Near-surface geophysics. Soc. Exploration Geophys. 31–70.

Komine, H., 1997. Evaluation of chemical grouted soil by electrical resistivity. Proc. Inst. Civil Eng. Ground Improv. 1, 101–113.

Kouretzis, G.P., Karamitros, D.K., Sloan, S.W., 2015. Analysis of buried pipelines subjected to ground surface settlement and heave. Can. Geotech. J. 52, 1058–1071.

Liu, S.Y., Du, Y.J., Han, L.H., Gu, M.F., 2008. Experimental study on the electrical resistivity of soil–cement admixtures. Environ. Geol. 54, 1227–1233.

Lyu, C., Sun, Q., Zhang, W., Hao, S., 2019. Effects of NaCl concentration on electrical resistivity of clay with cooling. J. Appl. Geophys. 170, 103843.

Ma, W., Wen, Z., Sheng, Y., Wu, Q.B., Wang, D.Y., Feng, W.J., 2012. Remedying embankment thaw settlement in a warm permafrost region with thermosyphons and crushed rock revetment. Can. Geotech. J. 49, 1005–1014.

Mao, Y., Romero Morales, E.E., Gens Solé, A., 2016. Exploring Ice Content on Partially Saturated Soils using Dielectric Permittivity and Bulk Electrical Conductivity Measurements, pp. 1–6.

Merifield, R.S., White, D.J., Randolph, M.F., 2009. Effect of surface heave on response of partially embedded pipelines on clay. J. Geotech. Geoenviron. 135, 819–829.

Ming, F., Li, D.Q., Chen, L., 2020. Electrical resistivity of freezing clay: experimental study and theoretical model. J. Geophys. Res. Earth Surf. 125, e2019JF005267.

NOAA, 2019. WFO Monthly/Daily Climate Data.

Oldenborger, G.A., LeBlanc, A.-M., 2018. Monitoring changes in unfrozen water content with electrical resistivity surveys in cold continuous permafrost. Geophys. J. Int. 215, 965–977.

Petrenko, V.F., 1993. Electrical properties of ice. US Army Corps of Engineers, Cold Regions Research & Engineering Laboratory.

Rucker, D.F., Schindler, A., Levitt, M.T., Glaser, D.R., 2009. Three-dimensional electrical resistivity imaging of a gold heap. Hydrometallurgy 98, 267–275.

Samouëlian, A., Cousin, I., Richard, G., Tabbagh, A., Bruand, A., 2003. Electrical resistivity imaging for detecting soil cracking at the centimetric scale. Soil Sci. Soc. Am. J. 67, 1319–1326.

Shan, W., Hu, Z., Guo, Y., Zhang, C., Liu, Y., 2017. Resistivity model of Frozen soil and high-density resistivity method for exploration discontinuous permafrost. Electrical Resistivity Conductivity 23.

Slater, L.D., Glaser, D.R., 2003. Controls on induced polarization in sandy unconsolidated sediments and application to aquifer characterization. Geophysics 68, 1547–1558.

Sreedeep, S., Reshma, A.C., Singh, D.N., 2005. Generalized relationship for determining soil electrical resistivity from its thermal resistivity. Exp. Thermal Fluid Sci. 29, 217–226.

Sudha, K., Israil, M., Mittal, S., Rai, J., 2009. Soil characterization using electrical resistivity tomography and geotechnical investigations. J. Appl. Geophys. 67, 74–79.

Sun, Q., Lyu, C., Zhang, W., 2020. The relationship between thermal conductivity and electrical resistivity of silty clay soil in the temperature range − 20 C to 10 C. Heat Mass Transf. 56, 2007–2013.

Sun, Z.Z., Ma, W., Zhang, S.J., Mu, Y.H., Yun, H.B., Wang, H.L., 2018. Characteristics of thawed interlayer and its effect on embankment settlement along the Qinghai-Tibet Railway in permafrost regions. J. Mt. Sci. 15, 1090–1100.

Supper, R., Ottowitz, D., Jochum, B., Römer, A., Pfeiler, S., Kauer, S., Keuschnig, M., Ita, A., 2014. Geoelectrical monitoring of frozen ground and permafrost in alpine areas: field studies and considerations towards an improved measuring technology. Near Surf. Geophys. 12, 93–115.

Tang, L., Wang, K., Jin, L., Yang, G., Jia, H., Taoum, A., 2018. A resistivity model for testing unfrozen water content of frozen soil. Cold Reg. Sci. Technol. 153, 55–63.

Wu, Y., Hubbard, S.S., Ulrich, C., Wullschleger, S.D., 2013. Remote monitoring of Freeze–Thaw transitions in Arctic soils using the Complex Resistivity Method. Vadose Zone J. 12, vzj2012.0062.

Wu, Y., Nakagawa, S., Kneafsey, T.J., Dafflon, B., Hubbard, S., 2017. Electrical and seismic response of saline permafrost soil during freeze - Thaw transition. J. Appl. Geophys. 146, 16–26.

Young, H.D., Freedman, R.A., Sandin, T.R., Ford, A.L., 1996. University Physics. Addison-Wesley New York.

Zhang, D., Cao, Z., Fan, L., Liu, S., Liu, W., 2014. Evaluation of the influence of salt concentration on cement stabilized clay by electrical resistivity measurement method. Eng. Geol. 170, 80–88.

Zhang, T., Barry, R.G., Knowles, K., Ling, F., Armstrong, R.L., 2002. Distribution of Seasonally and Perennially Frozen Ground in the Northern Hemisphere. AA Balkema Publishers Zürich, Switzerland, pp. 1289–1294.

Zhao, L., Ping, C.-L., Yang, D., Cheng, G., Ding, Y., Liu, S., 2004. Changes of climate and seasonally frozen ground over the past 30 years in Qinghai–Xizang (Tibetan) Plateau, China. Glob. Planet. Chang. 43, 19–31.

Zhou, Q.Y., Shimada, J., Sato, A., 2001. Three-dimensional spatial and temporal monitoring of soil water content using electrical resistivity tomography. Water Resour. Res. 37, 273–285.

REPORT DOCUMENTATION PAGE

1. REPORT DATE April 2024	2. REPORT TYPE Final Report	3. DATES COVERED	
		START DATE	END DATE

4. TITLE AND SUBTITLE

Experimental and Numerical Analyses of Soil Electrical Resistivity under Subfreezing Conditions

5a. CONTRACT NUMBER W913E518C0008	5b. GRANT NUMBER	5c. PROGRAM ELEMENT PE 0602784A
5d. PROJECT NUMBER T53	5e. TASK NUMBER 08	5f. WORK UNIT NUMBER

6. AUTHOR(S)

Rui Liu, Cheng Zhu, John Schmalzel, Daniel Offenbacker, Yusuf Mehta, Benjamin Barrowes, Danney Glaser, and Wade Lein

7. PERFORMING ORGANIZATION NAME(S) AND ADDRESS(ES) See reverse.	8. PERFORMING ORGANIZATION REPORT NUMBER ERDC/CRREL MP-24-2

9. SPONSORING/MONITORING AGENCY NAME(S) AND ADDRESS(ES) US Army Corps of Engineers Washington, DC 20314-1000	10. SPONSOR/MONITOR'S ACRONYM(S)	11. SPONSOR/MONITOR'S REPORT NUMBER(S)

12. DISTRIBUTION/AVAILABILITY STATEMENT

Distribution Statement A. Approved for public release: distribution is unlimited.

13. SUPPLEMENTARY NOTES

This paper was originally published as R. Liu, C. Zhu, J. Schmalzel, D. Offenbacker, Y. Mehta, B. Barrowes, D. Glaser, and W. Lein, "Experimental and Numerical Analyses of Soil Electrical Resistivity under Subfreezing Conditions," *Journal of Applied Geophysics* 202 (July 2022): 104671, https://doi.org/10.1016/j.jappgeo.2022.104671.

14. ABSTRACT

The engineering behavior of frozen soils is critical to the serviceability of civil infrastructure in cold regions. Among various geophysical techniques, electrical resistivity imaging is a promising technique that is cost effective and provides spatially continuous subsurface information. In this study, under freeze–thaw conditions, we carry out lab–scale 1D electrical resistivity measurements on frost–susceptible soils with varying water content and bulk density properties. We use a portable electrical resistivity meter for temporal electrical resistivity measurements and thermocouples for temperature monitoring. Dynamic temperature-dependent soil properties, most notably unfrozen water content, exert significant influences on the observed electrical resistivity. Below 0 °C, soil resistivity increases with the decreasing temperature. We also observe a hysteresis effect on the evolution of electrical resistivity during the freeze–thaw cycle, which effect we characterize with a sigmoidal model. At the same temperature, electrical resistivity during freezing is consistently lower than that during thawing. We have implemented this sigmoidal model into a COMSOL finite element model at both laboratory and field scales which enables the simulation of soil electrical resistivity response under both short–term and long–term sub–freezing conditions. Atmospheric temperature variations induce soil temperature change, and thereby phase transition and electrical resistivity change, with the rate of change being a function of the depth of investigation and soil properties include initial water content and initial temperature. This study advances the fundamental understanding of the electrical behaviors of frozen soils and enhance the application of electrical geophysical investigations in cold regions.

15. SUBJECT TERMS

Frozen soil, Electrical resistivity, Finite element modeling, Freeze–thaw

16. SECURITY CLASSIFICATION OF:			17. LIMITATION OF ABSTRACT SAR	18. NUMBER OF PAGES 21
a. REPORT Unclassified	b. ABSTRACT Unclassified	C. THIS PAGE Unclassified		

19a. NAME OF RESPONSIBLE PERSON	19b. TELEPHONE NUMBER (include area code)

7. PERFORMING ORGANIZATION NAME(S) AND ADDRESS(ES) (concluded)

US Army Engineer Research and Development Center (ERDC)
Cold Regions Research and Engineering Laboratory (CRREL)
72 Lyme Road
Hanover, NH 03755-1290

Rowan University
Center for Research and Education in Advanced Transportation Engineering Systems (CREATEs)
Department of Civil and Environmental Engineering
201 Mullica Hill Road
Glassboro, New Jersey 08028

Rowan University
Department of Electrical and Computer Engineering
201 Mullica Hill Road
Glassboro, New Jersey 08028